Long-range Fourier domain optical coherence tomography of the pediatric subglottis

Veronika Volgger, MD[a,1], **Giriraj K. Sharma, MD, MS**[b,*,1], **Joe Jing, MS**[c], **Ya-Sin A. Peaks, MD, MBA, MS**[b], **Anthony Chin Loy, MD**[b], **Frances Lazarow, MD**[b], **Alex Wang, MS**[d], **Yueqiao Qu, BS**[c], **Erica Su, BS**[d], **Zhongping Chen, PhD**[d], **Gurpreet S. Ahuja, MD**[b,e], and **Brian J-F. Wong, MD, PhD**[b]

[a]Department of Otorhinolaryngology – Head and Neck Surgery, Ludwig Maximilian University Munich, 80539 München, Germany

[b]Department of Otolaryngology – Head and Neck Surgery, University of California Irvine, Orange, CA 92868, USA

[c]Department of Biomedical Engineering, University of California Irvine, Irvine, CA 92612, USA

[d]Beckman Laser Institute, University of California Irvine, Irvine, CA 92612, USA

[e]CHOC Children's Hospital of Orange County, Orange, CA 92868, USA

Abstract

Background—Acquired subglottic stenosis (SGS) most commonly results from prolonged endotracheal intubation and is a diagnostic challenge in the intubated child. At present, no imaging modality allows for *in vivo* characterization of subglottic microanatomy to identify early signs of acquired SGS while the child remains intubated. Fourier domain optical coherence tomography (FD-OCT) is a minimally invasive, light-based imaging modality which provides high resolution, three dimensional (3D) cross-sectional images of biological tissue. We used long-range FD-OCT to image the subglottis in intubated pediatric patients undergoing minor head and neck surgical procedures in the operating room.

Methods—A long-range FD-OCT system and rotary optical probes (1.2 mm and 0.7 mm outer diameters) were constructed. Forty-six pediatric patients (ages 2–16 years) undergoing minor upper airway surgery (e.g. tonsillectomy, adenoidectomy) were selected for intraoperative, trans-endotracheal tube FD-OCT of the subglottis. Images were analyzed for anatomical landmarks and subepithelial histology. Volumetric image sets were rendered into virtual 3D airway models in Mimics software.

*Corresponding Author: Giriraj K. Sharma, MD, MS, Beckman Laser Institute, 1002 Health Science Road, Irvine, CA 92612, Phone: +1-703-585-3162, giriraj112@gmail.com.
[1]V.V. and G.K.S. are co-first authors

Results—FD-OCT was performed on 46 patients (ages 2–16 years) with no complications. Gross airway contour was visible on all 46 data sets. Twenty (43%) high-quality data sets clearly demonstrated airway anatomy (e.g., tracheal rings, cricoid, vocal folds) and layered microanatomy of the mucosa (e.g., epithelium, basement membrane, lamina propria). The remaining 26 data sets were discarded due to artifact, high signal-to-noise ratio or missing data. 3D airway models allowed for user-controlled manipulation and multiplanar airway slicing (e.g. sagittal, coronal) for visualization of OCT data at multiple anatomic levels simultaneously.

Conclusions—Long-range FD-OCT produces high-resolution, 3D volumetric images of the pediatric subglottis. This technology offers a safe and practical means for *in vivo* evaluation of lower airway microanatomy in intubated pediatric patients. Ultimately, FD-OCT may be applied to serial monitoring of the neonatal subglottis in long-term intubated infants at risk for acquired SGS.

Keywords

Optical coherence tomography; subglottis; subglottic stenosis; pediatrics

1. INTRODUCTION

Acquired subglottic stenosis (SGS) in a neonate or child is most commonly a result of prolonged endotracheal intubation for mechanical ventilation [1]. In these intubated patients, the endotracheal tube (ETT) may impose pressure and/or exert a shearing effect against the delicate and pliable subglottic mucosa. This may induce necrosis and trigger a wound healing cascade which, if undiagnosed, culminates in granulation and stenosis [2–4]. Furthermore, the cricoid is the only complete cartilaginous ring of the pediatric airway, preventing airway expansion in the event of subglottic injury and edema [4–6]. While the current incidence of acquired SGS in neonatal intensive care unit (NICU) settings is approximately 0.24–3.0% [6–8], SGS remains a diagnostic and therapeutic challenge for otolaryngologists. High-grade SGS often requires multi-staged surgical intervention which is associated with increased morbidity and risk for long-term voice impairment or dysphonia [9, 10].

At present, clinicians have limited options for diagnosing SGS. High-resolution computed tomography (CT) has spatial resolution up to 0.5 mm, but exposes patients to ionizing radiation [11]. Direct laryngoscopy and rigid endoscopy remains the gold standard for diagnosis of SGS. However, this procedure is often performed after patients fail extubation in the ICU with clinical or radiographic signs of SGS. By this point, mature scar tissue has often developed, requiring endoscopic or open surgical intervention. Furthermore, rigid endoscopy is limited to a visual assessment of the luminal dimensions and mucosal surface of the airway, entails the use of general anesthesia and carries risk of mucosal trauma from airway instrumentation. Hence, there exists a need for a less invasive imaging modality with the capability of evaluating the substructural anatomy of subglottic tissues while children are intubated. This may help identify early signs of epithelial and subepithelial injury secondary to the ETT and alert the otolaryngologist and intensivist prior to the onset of fibrosis and cicatrization.

Optical coherence tomography (OCT) is a minimally invasive imaging modality that couples non-ionizing near infrared light (laser or super luminescent LED) with principles of low coherence interferometry [12]. OCT acquires high resolution (~10 μm), three dimensional (3D) cross sectional images of living tissue at video rate imaging speeds. OCT is analogous to ultrasound B-mode imaging, however instead of measuring acoustic echoes, OCT measures back-reflectance of light from biological tissue (up to 2 mm penetration depth) based on optical scattering properties of tissue structures. Previous reports have described OCT of the neonatal and pediatric subglottis [13, 14]. However, these studies used time-domain (TD-OCT) systems which were limited by slow imaging speeds (0.33 frames/sec) and linear, two-dimensional (2D) image acquisition methods. A derivative of conventional OCT, known as anatomic or long-range OCT, has been shown to image airway lumens up to 30–40 mm in diameter [15, 16]; systems used in these studies also had low imaging speeds (1–5 frames/sec). Frequency, or "Fourier", domain swept source OCT (FD-OCT) is an advanced OCT technology which exhibits higher sensitivity and imaging speeds (25 frames/sec) than TD-OCT systems, allowing for real-time, dynamic monitoring of the airway. In 2012, Jing et al. described *in vivo* high-speed long-range FD-OCT of the adult upper airway [17]. Their system utilized a rotary endoscopic probe which allowed 360° scanning of the airway (axial imaging range ~15 mm) and demonstrated the capability of long-range FD-OCT to acquire anatomic and substructural images of the airway in a 3D volumetric format. Additional reports of swept source anatomical OCT imaging of *ex vivo* (swine) airways and pediatric airway phantoms in a volumetric format (helical scanning) are available in literature [18, 19]. Those FD-OCT systems consisted of a fiber-optic probe integrated with a small-bore flexible endoscope for quantification of airway lumen geometry.

The objective of this study was to evaluate the feasibility and methodology of long-range FD-OCT imaging of the subglottis in intubated children undergoing minor upper airway surgery. A controlled, operative setting with adequate personnel and resources for airway management allowed for safe evaluation of trans-ETT OCT imaging of the airway and simulation of bedside OCT imaging of intubated patients. While the patients included in this study were not at risk for acquired SGS, FD-OCT was used to identify normal structural microanatomy within the subglottis. This is the first report of *in vivo* long-range (~9 mm axial imaging range) FD-OCT in the pediatric lower airway. This investigation is a step towards the use of long-range FD-OCT in the NICU to acquire volumetric images of the intubated neonatal airway. In anticipation of this future application, the current study served as a pilot to optimize specifications of the OCT sampling probe and trans-ETT imaging methodology.

2. MATERIAL AND METHODS

2.1 Study Design

Approval for this study was obtained from the human subjects Institutional Review Board at the University of California Irvine (HS# 2003-3025) and Children's Hospital of Orange County (IRB #1211115). We conducted a prospective clinical trial to evaluate long-range FD-OCT of the subglottis in pediatric patients undergoing minor upper airway surgery (e.g. tonsillectomy, adenoidectomy). The study was temporally divided into two phases (Phase I

and II); alterations to OCT probe design, rotational and translational speeds were made between phases. All patients reported no history of subglottic injury or prolonged endotracheal intubation. Patient age, weight and pertinent medical history were recorded from the medical record.

2.2 OCT system

A long-range swept source FD-OCT system was designed and constructed (Figure 1a). The interferometry unit specifications are previously described [17]. Near-infrared light is generated from a 1310 nm swept source laser (Axsun Technology, Billerica, MA, USA) operating at 50 kHz A-line scan rate. Light is split by a 90:10 coupler into a sample arm (biological tissue) and reference arm (mirror), respectively. In the reference arm, an acousto-optic modulator (AOM; Brimrose, Sparks, MD, USA) generates a frequency shift (150 MHz) which allows for the removal of mirror terms that arise from Fourier transform processing and utilization of the complete coherence length of the laser. For our system, this amounts to an increase in imaging range by a factor of 2, as compared to a standard OCT system utilizing the same light source. The 6 dB system sensitivity range as measured with a collimated beam in the sample arm was reported previously to be 12.8 mm [20]. Based on unique optical scattering properties of tissue structures, OCT signal is back-reflected from the sample arm and recombined with the reference arm to generate a reflectivity profile (A-line).

Two thousand A-lines are aligned to form a single frame, with axial resolution of approximately 10 μm. Two types of custom-built, flexible endoscopic OCT probes (75–80 cm length) were constructed with outer diameters (OD) of 1.2 mm (Phase I) and 0.7 mm (Phase II). In Phase II of the study, a slimmer probe was built to simulate trans-ETT imaging of the neonatal subglottis. In NICU settings, endotracheal intubation is typically conducted with uncuffed 2.5 to 3.5 Fr ETTs. Hence, 0.7 mm OD probes more suitable for the luminal dimensions of neonatal ETTs and ventilation circuits were tested.

Probes consisted of a single-mode optical fiber encased in a stainless torque coil (Asahi Intecc; Santa Clara, CA, USA). Fibers were coupled distally with a gradient refractive index (GRIN; Go!Foton, Somerset, NJ, USA) lens used to focus the laser beam on a 45-degree gold-coated mirror which reflected the signal at a 90-degree angle. The GRIN lens and mirror were enclosed in a custom designed metal housing to protect these fragile components (Figure 1b). The 1.2 mm OD probe had a focal length of ~9 mm and a Rayleigh range of 5.2 mm. The 0.7 mm OD probe had a focal length of ~3 mm and a Rayleigh range of 850 μm. While the reduced Rayleigh range of the smaller probe reduces the overall imaging range, these probes were designed to cover the majority of radial distances to tissue surfaces encountered in the neonatal subglottic airway. The overall sensitivity roll off with respect to depth for the FD-OCT system and a 9 mm focal length probe is shown in Figure 2. A 6 dB sensitivity roll-off is demonstrated at a total imaging range of 8 mm which is less than the system sensitivity due to the focal length and Rayleigh range of the probe. The combined imaging range of the system could be increased by increasing the focal length of the probe however at the cost of a reduced lateral resolution.

Rotational scanning of the OCT probe was accomplished using an external rotational motor (Animatics; Santa Clara, CA, USA) coupled to a fiber optic rotary joint (Princetel Inc.; Pennington, NJ, USA). Torque from the rotational motor was translated through the coil to the distal probe tip. A dual-motor stage (Zaber Technologies Inc.; Vancouver, BC, Canada) allowed for simultaneous linear pullback of the probe along the longitudinal axis of the airway, thus allowing for image acquisition in a helical, retrograde fashion. Rotation and pullback speeds were customizable to adjust the z-axis separation between adjacent 360° frames.

2.3 OCT imaging

Non-contact FD-OCT imaging was conducted in the operating room (OR). The OR setup, including ventilation circuit and OCT hardware, is illustrated in Figure 3. Patients were placed in supine position and general anesthesia was administered with endotracheal intubation. Trans-ETT FD-OCT imaging of the lower airway was conducted before starting the planned surgical procedure. Standard mechanical ventilation settings, sedative and analgesic medications were maintained during FD-OCT imaging. Probe rotation and pullback, data acquisition and real-time image display were controlled by Windows-based software.

The ETT was copiously suctioned by the anesthesiologist to clear airway secretions. OCT probes were encased in a transparent and sterilized fluorinated ethylenepropylene (FEP) sheath (Zeus Inc.; Orangeburg, SC, USA). Sheaths were distally-sealed with ultraviolet (UV) glue (early Phase I) or heat-sealed with a butane lighter (late Phase I, Phase II). In the first 6 cases of Phase I, ventilation was temporarily interrupted to insert a pediatric flexible laryngoscope along with the sheath (housing the OCT probe) through the ETT. In these cases, we consistently visualized the distal ETT tip in the proximal trachea, the desired starting point for imaging. Hereafter, to minimize ventilation disruption and general anesthesia time, endoscopic visualization of probe placement was eliminated. In the subsequent 40 cases, a Bodai double swivel connector (Tri-anim Health Services; Dublin OH, USA) was inserted between the ETT and ventilation circuit to create a point of entry for the OCT probe. The length of the ETT (intra-and extra-oral) and connector were measured and added to establish the distance to advance the sheath through the ventilation circuit.

During Phase I (n=31), a 1.2 mm OD probe housed in a 2.08 mm OD sheath was used for trans-ETT imaging. The sheath was inserted through the Bodai connector aperture (Figure 3) and advanced inside the ETT until the probe tip reached 5 mm proximal to the ETT tip (per calculated distance). At all points during the case, the FEP sheath remained within the lumen of ventilation circuit and ETT, and did not come into direct contact with airway tissue. The probe was rotated (25 Hz) and linearly retracted (3.13 mm/sec) within the sheath to acquire 360° images in a helical fashion with 125 μm separation between consecutive frames. Image acquisition started in the proximal trachea and terminated in the supraglottic space. The sheath was held stationary within the ETT during probe pullback. Upon completion, the probe was reinserted to the distal end of the sheath to acquire 1–2 additional data sets (6–8 Gb total data).

During Phase II (n=15), a 0.7 mm OD probe, encased in a 1.37 mm OD sheath, was inserted into the ETT in a manner identical to Phase I. Slower rotational speed (12.5 Hz) and linear translation speed (1.56 mm/sec) were used to minimize mechanical stress on the smaller and more delicate probe. Phase II volumetric data had 125 μm separation between consecutive 360° frames. Two to three total data sets per patient were acquired in this fashion.

The time to acquire one set of OCT images from the laryngotracheal complex was approximately 20–30 seconds. Overall procedural time including equipment setup and data acquisition was between 3 to 4 minutes. Following image acquisition, the probe and sheath were withdrawn from the airway and the planned surgical procedure was started.

2.4 Data analysis

Continuous helical scanning of the airway generated 300–600 360° raw images (BMP file format; 2000×2048 pixels) in Cartesian coordinates. Offline data analysis included frame-by-frame examination of OCT data within a graphic viewer (IrfanView; Irfan Skiljan, Austria). To identify airway anatomy, OCT data was first converted from Cartesian to polar coordinates using software coded in MATLAB (MathWorks; Natick, MA, USA). This rendered the data into an anatomic (axial) configuration for ease of visualization and analysis. Data was first inspected for signal strength, optical penetration depth, noise levels and image distortion. Data sets with easily recognizable tissue contours and anatomical structures were analyzed for mucosal microanatomy. Airway levels were identified based on distinct topographical characteristics and locations of anatomical structures (e.g., cartilage, vocal folds). Subglottic mucosal microstructure (e.g., epithelium, basement membrane, lamina propria) was identified based on differences in greyscale intensity, correlating to unique optical properties of each tissue layer.

2.5 3D airway modeling

Detailed description of image post-processing and 3D reconstruction of laryngotracheal airway models are described previously [21]. Post-processing of raw OCT image stacks was conducted in IrfanView, MATLAB and Amira (FEI Visualization Science Group; Burlington, MA, USA). Major steps included: 1) frame height correction to portray correct airway diameter, 2) image conversion from Cartesian to polar coordinates, 3) frameshift alignment and 4) image downsizing. Frameshift alignment involved correction for spatial shifting between consecutive 360° frames, caused by movement of the probe tip during high-speed rotation within the sheath. Processed images were imported into Mimics (Materialise; Leuven, Belgium) for 3D rendering. User-defined spatial filters delineated airway mucosa from cartilage, excess noise, artifact or hardware (e.g., sheath, ETT). Processed 2D images in polar coordinates were stacked and rendered into 3D airway models. Within Mimics, user-controlled slicing of the 3D airway in axial, sagittal or coronal orientations allowed for cross-sectional visualization of OCT data at multiple anatomic levels.

3. RESULTS

Intraoperative long-range FD-OCT was performed in 46 subjects (ages 2–16 years, mean weight 25.2 kg). Phase I included 31 cases and Phase II included 15 cases. Nineteen patients were male and 26 were female. All 46 cases were performed to completion, without any adverse physiologic events. In all cases, mechanical ventilation was not interrupted and there were no episodes of oxygen desaturation during the OCT portion of the case.

3.1 OCT data

All 46 data sets demonstrated the gross contour of the laryngotracheal complex. Twenty of 46 (43%) cases yielded high-quality OCT images which clearly depicted tissue planes within the mucosa including epithelium, basement membrane and lamina propria. Structural features such as perichondrium, cartilage, vocal folds and laryngeal ventricles were also identified, which aided in defining airway levels (e.g., larynx, subglottis, trachea) within the image stack. Twenty-six data sets were discarded due to unfavorable signal:noise ratio, inadequate optical penetration depth, or segments of grossly distorted or missing data. All patients included in this study had no history of subglottic disease or prolonged endotracheal intubation. Therefore, all OCT data sets and digital 3-D airway models acquired in this study demonstrated normal microanatomy of the subglottic airway.

As light propagates through tissue, photons are absorbed, scattered or backscattered depending on the unique optical properties (e.g., scattering, absorption, anisotropy) of tissue elements. Within a reflectivity profile, turbid media (e.g., biological tissue) is represented as a heterogeneous configuration of grayscale intensities. Media with low turbidity (e.g., water or the lumen of a gland) cause zero to minimal backscattering of light, and appear as dark pixels. Dense, highly scattering tissue such as cartilage surface or gastric secretions reflect signal at higher intensities, and appear as near-white or white pixels.

Figure 4 shows a representative OCT image of a pediatric (age = 7 years) trachea acquired during Phase I (1.2 mm probe). When visualized in polar coordinates (Figure 4a), the classic "D" shaped cross-sectional contour of the trachea is noted. Subepithelial structures, defined by the unique greyscale intensities of each mucosal layer, are more easily visualized when data is represented in Cartesian coordinates (Figure 4b). The bright lines present in the images are artifacts, which arise from saturation of the photodetector due to large specular reflections off the protective sheath either at a particular bend angle or from accrued moisture on the sheath surface. An OCT image of the subglottis from the same patient is shown in Figure 5. This set of images shows the ovoid cross-sectional contour of the subglottis (Figure 5a). Compared to tracheal mucosa, the subglottis OCT image depicts a marginally thicker lamina propria layer (Figure 5b).

Matched polar and Cartesian images of the subglottis of a 2 year old patient are shown in Figure 6. In this Phase II case, the 0.7 mm probe produced less axial noise than the previously described examples. However, hysteresis followed by recoil of the probe during high-speed rotation resulted in artificial stretching of a segment of A-lines (white box). This example demonstrates how the slightest convolution of the coil during rotation translates to image distortion of far greater magnitude. High-quality images from Phase I (1.2mm probe)

and Phase II (0.7 mm probe) had no noticeable difference in overall signal strength, noise levels or degree of artifact.

3.2 3D airway modeling

3D airway models were constructed in Mimics as a cylindrical tube with OCT pixels (segmented mucosa) constituting the airway wall. Figure 7 shows sagittal, oblique and superior views of a 3D airway model reconstructed from data acquired from a 6 year old patient. In Figure 8, sagittal, coronal and axial cross-sectional views of the same 3D model are shown. These representations are a result of user-controlled slicing of the 3D model to visualize OCT data along the full length of the laryngotracheal complex. Cross-sectional views of the airway depict the normal layered microanatomy of the subglottis in 3D.

4. DISCUSSION

This is the first report of *in vivo* long-range FD-OCT of the pediatric subglottis. The high-speed, helical imaging mechanism of our FD-OCT probe yielded 3D anatomical and structural images of the pediatric subglottis. Hereby, we are also the first to demonstrate OCT-based 3D digital reconstruction of the pediatric laryngotracheal airway. The technology and methods described here are a major step towards our long-term goal of applying long-range FD-OCT to monitor the intubated neonatal airway. We aimed to identify potential obstacles with bedside imaging in a NICU setting and refine our technology platform to improve the consistency of image quality.

The OCT technique described in this study allows for non-contact imaging of the laryngotracheal airway in intubated patients. This method is minimally invasive as the patient remains intubated and ventilated throughout the case, no additional sedative or analgesic medications are required and there is no direct contact between the OCT probe and airway tissue. In a pediatric ICU or NICU setting, no manipulation or repositioning of the patient would be necessary given that the access point (Bodai connector) of the OCT probe is external to the patient's body (Figure 3). FD-OCT offers major advantages over current modes of *in vivo* airway imaging including fly-through CT bronchoscopy (radiation risk, limited resolution) or rigid endoscopy (general anesthesia, need for extubation). OCT advantages include: 1) high-resolution imaging (~10 μm) which delineate subepithelial microanatomy, 2) the potential for early diagnosis of occult subglottic histopathology prior to the onset of mature scar formation and airway-compromising stenosis, 3) imaging depth up to 2 mm, as opposed to endoscopic surface views of the mucosa offered by bronchoscopy and 4) trans-ETT imaging, which precludes the need for temporary extubation and operative endoscopy, a contact or near-contact diagnostic procedure which may cause mucosal abrasion.

4.1 OCT images and 3D models

While OCT images from all 46 cases depicted the contour of the airway wall, only 20 (43%) image sets clearly delineated the layered, subepithelial microanatomy of the subglottis. Data quality on the remaining 26 data sets was compromised by noise, abstract and/or limited optical penetration depth. Therefore, imaging yield was highly dependent on the clarity and

strength of OCT signal from the probe. Given the microscopic scale and precision involved in optical probe fabrication, we experienced variability in signal quality and noise levels. Furthermore, during high-speed rotation of the probe within the sheath, wavering of the distal probe tip and friction between the coil and sheath leads to shifting and stretching of the data, respectively. Additionally, any airway secretions which remained within the ETT after suctioning added to signal interference.

We noted no major differences in image quality between Phase I and Phase II data. However, the 0.7 mm probes (Phase II) were constructed using a smaller gauge fiber, GRIN lens and mirror, causing these probes to lose signal quality more rapidly or break more frequently with repeat usage. Hence, the yield for high-quality data was slightly lower in the beginning of Phase II. To increase the longevity of the 0.7 mm probes, we reduced the rotational speed to moderate the torque and mechanical stress applied to the probe. Of note, internal misalignment or damage of the probe optical assembly (e.g. fiber, grin lens, mirror) were always sustained within the confines of the torque coil or metal housing. Because probes were maintained in distally-sealed protective sheaths, it is impossible for optical elements to disengage into the airway and hence, probe damage did not pose risk to patients.

Within Mimics, 3D airway models allowed for user-controlled slicing and examination of the airway mucosa. While airway renderings were based on normal airway anatomy in the current study, visualization of the layered microanatomy in 3D (Figure 8) confers the ability to evaluate substructural irregularities correlating with injury at multiple airway levels simultaneously. In airways with subglottic scar tissue secondary to long-term endotracheal intubation, we believe 3D models would allow clinicians to spatially and precisely identify the location and length of these pathological changes.

The data obtained in this study demonstrates promise for quantitative image analysis and future clinical applications. Identification of subglottic histopathology secondary to endotracheal intubation has been demonstrated from OCT data previously [14]. Pathologic changes such as glandular dilatation, edema or fibrosis were distinguished from normal tissue based on focal disparities in grey-scale intensity. Digital analysis of the intensity or "texture" properties within such regions of fibrosis may provide a quantitative metric for diagnosing the extent or type of scar tissue. Furthermore, digital segmentation and depth measurement of select tissues such as the entire mucosa, individual substructural layers (e.g. lamina propria) or a segment of scar tissue can be accomplished using the ETT wall as a measurement reference within the OCT frame. Morphometric analysis of the depth of scar tissue may provide valuable objective data in planning surgical intervention (e.g. slide tracheoplasty vs. tracheal resection). Lastly, 3D airway renderings can potentially identify the length, radial distribution and location (relative to vocal folds) of scar tissue to further assist the otolaryngologist in planning surgical therapy (e.g., cricotracheal resection vs. laryngotracheal resection) and formulating an individualized treatment plan. We plan to evaluate all aforementioned image analysis methods in future studies of intubated neonatal and pediatric patients at risk of developing SGS.

4.2 Procedural refinement

The controlled environment of the OR was an ideal setting to define challenges and fine-tune our methodology while ensuring patient safety. As the otolaryngology team conducted OCT imaging, the anesthesiologist and OR nurses were present at bedside to assist in airway management. Synergy and clear communication amongst the entire team ensured everyone understood the procedure and potential risks (e.g., oxygen desaturation, apnea, airway compromise) and could vocalize if the child was not ventilating adequately at any point during the case. This is especially critical in a NICU setting, considering the decreased pulmonary reserve of the neonate and smaller caliber ETTs and ventilation circuits used in NICUs.

At the completion of one case, we noted that the distal seal of the sheath had broken, extricating a piece of UV glue into the pulmonary tree. While this did not cause any adverse physiologic event, such a foreign body has potential to cause desaturation or trigger an apneic episode in the pre-term or term neonate. From this point forward (remainder of Phase I and Phase II), all sheaths were heat-sealed to ensure there were no loose parts in our sampling arm.

Suctioning of the ETT was performed before and, if necessary, between imaging sets to minimize signal interference. Despite these efforts, early in our study, airway secretions sporadically entered the lumen of the sheath through minute fissures in the sealed distal end. This resulted in blockage of the OCT signal and, in rare cases, permanent damage to the probe. Thereafter, we tested the integrity of the seal for air leaks underwater and thus increased the longevity of our probes. We also learned to prevent sheath kinks and to minimize the curvature of the probe outside the ventilation circuit (between the rotational motor and Bodai connector) to allow unrestricted, high-speed rotation of the coil. If overlooked, these details had considerable effect on image quality, as the slightest hysteresis in probe rotation causes perceptible distortion of A-lines.

4.3 Limitations

While OCT-based volumetric and mucosal thickness measurements may be possible, the gold standards of CT and histology were not used as validation measures. However, numerous studies have compared anatomic OCT of the airway with CT to underscore the diagnostic sensitivity of OCT for volumetric imaging of the airway [17, 22, 23]. Lin et al. reported *in vivo* FD-OCT of the rabbit subglottis following brush injury to airway epithelium, followed by histologic section [24]. Their study demonstrated the diagnostic sensitivity of FD-OCT in identifying and characterizing tissue planes within the subglottic mucosa. Additional studies comparing OCT and histology demonstrate the validity of OCT-based measurements of airway mucosal thickness in animal models [25, 26] and human tissue [27].

4.4 Future steps

A variety of animal models of subglottic stenosis exist, of which a select cohort are listed here [28–32]. However, there are few reports of *in vivo* OCT of subglottic stenosis models with comparative histologic analysis [24]. Further validation of OCT with comparative

histology is warranted to evaluate OCT-based characterization of ETT injury and morphometric change within subglottic mucosa. As we progress towards using long-range FD-OCT to image the neonatal subglottis, a number of steps can be taken to improve image quality and efficiency of data analysis. As signal strength is fundamental to generating high-quality images, adopting a standardized probe fabrication protocol would improve image consistency and minimize loss of data. Currently in development by our group, algorithms for automated tissue surface recognition, segmentation and morphometric analysis (mucosal thickness, airway cross-sectional area) would allow efficient computation of gigabytes of data and readily provide clinicians with information on the dimensions and mucosal state of the subglottis. In future NICU-based OCT trials, we aim to serially image intubated neonates and use OCT data to evaluate for changes in lamina propria thickness (secondary to edema or scarring) with prolonged intubation. Lastly, our group is currently developing algorithms to analyze tissue texture properties. We hope quantitative texture analysis based on patterns in OCT image pixels would ultimately differentiate between normal lamina propria, edematous tissue and fibrosis.

5. CONCLUSIONS

Long-range swept source FD-OCT generates high-resolution, 3D volumetric images of the pediatric airway. FD-OCT allows for evaluation of subglottic microanatomy and 3D reconstruction of airway mucosa. We anticipate FD-OCT will allow for *in vivo* serial monitoring of the intubated neonatal airway. Identifying occult, subepithelial pathology of the subglottis may help neonatologists better manage the airway and reduce the incidence of subglottic ulceration and scarring which leads to SGS.

Acknowledgments

References

1. Hawkins DB. The Laryngoscope. 1977; 87:339–346. [PubMed: 839929]

2. Wei JL, Bond J. Current opinion in otolaryngology & head and neck surgery. 2011; 19:474–477. [PubMed: 21986802]

3. Whited RE. The Laryngoscope. 1985; 95:1216–1219. [PubMed: 4046708]

4. Hawkins DB. The Annals of otology, rhinology, and laryngology. 1987; 96:116–117.

5. Sherman JM, Lowitt S, Stephenson C, Ironson G. The Journal of pediatrics. 1986; 109:322–327. [PubMed: 3734970]

6. Holinger PH, Kutnick SL, Schild JA, Holinger LD. The Annals of otology, rhinology, and laryngology. 1976; 85:591–599.

7. Choi SS, Zalzal GH. Otolaryngology--head and neck surgery : official journal of American Academy of Otolaryngology-Head and Neck Surgery. 2000; 122:61–63. [PubMed: 10629484]

8. Walner DL, Loewen MS, Kimura RE. The Laryngoscope. 2001; 111:48–51. [PubMed: 11192899]

9. Clary RA, Pengilly A, Bailey M, Jones N, Albert D, Comins J, Appleton J. Archives of otolaryngology--head & neck surgery. 1996; 122:1189–1194. [PubMed: 8906053]

10. Brehm SB, Weinrich B, Zieser M, Kelchner L, Middendorf J, Elluru R, de Alarcon A. International journal of pediatric otorhinolaryngology. 2009; 73:1019–1023. [PubMed: 19410304]

11. Brenner DJ, Hall EJ. The New England journal of medicine. 2007; 357:2277–2284. [PubMed: 18046031]

12. Huang D, Swanson EA, Lin CP, Schuman JS, Stinson WG, Chang W, Hee MR, Flotte T, Gregory K, Puliafito CA, et al. Science. 1991; 254:1178–1181. [PubMed: 1957169]

13. Ridgway JM, Ahuja G, Guo S, Su J, Mahmood U, Chen Z, Wong B. The Laryngoscope. 2007; 117:2206–2212. [PubMed: 18322424]

14. Ridgway JM, Su J, Wright R, Guo S, Kim DC, Barretto R, Ahuja G, Sepehr A, Perez J, Sills JH, Chen Z, Wong BJ. The Annals of otology, rhinology, and laryngology. 2008; 117:327–334.

15. Armstrong J, Leigh M, Walton I, Zvyagin A, Alexandrov S, Schwer S, Sampson D, Hillman D, Eastwood P. Optics express. 2003; 11:1817–1826. [PubMed: 19466064]

16. Lau B, McLaughlin RA, Curatolo A, Kirk RW, Gerstmann DK, Sampson DD. Optics express. 2010; 18:27173–27180. [PubMed: 21196994]

17. Jing J, Zhang J, Loy AC, Wong BJ, Chen Z. Journal of biomedical optics. 2012; 17:110507. [PubMed: 23214170]

18. Wijesundara, KC.; Iftimia, NV.; Oldenburg, AL. Proceedings - Society of Photo-Optical Instrumentation Engineers; 2013; p. 8571

19. Wijesundara K, Zdanski C, Kimbell J, Price H, Iftimia N, Oldenburg AL. Biomedical optics express. 2014; 5:788–799. [PubMed: 24688814]

20. Chou L, Batchinsky A, Belenkiy S, Jing J, Ramalingam T, Brenner M, Chen Z. Journal of biomedical optics. 2014; 19:36018. [PubMed: 24664245]

21. Su, E.; Sharma, G.; Chen, J.; Nguyen, T.; Wang, AAH.; Ahuja, G.; Chen, Z.; Wong, B. Proceedings of SPIE; 2014; 2014. p. 8926

22. Williamson JP, Armstrong JJ, McLaughlin RA, Noble PB, West AR, Becker S, Curatolo A, Noffsinger WJ, Mitchell HW, Phillips MJ, Sampson DD, Hillman DR, Eastwood PR. The European respiratory journal. 2010; 35:34–41. [PubMed: 19541718]

23. Armstrong JJ, Leigh MS, Sampson DD, Walsh JH, Hillman DR, Eastwood PR. American journal of respiratory and critical care medicine. 2006; 173:226–233. [PubMed: 16239620]

24. Lin JL, Yau AY, Boyd J, Hamamoto A, Su E, Tracy L, Heidari AE, Wang AH, Ahuja G, Chen Z, Wong BJ. JAMA otolaryngology-- head & neck surgery. 2013; 139:502–509. [PubMed: 23681033]

25. Mahmood U, Hanna NM, Han S, Jung WG, Chen Z, Jordan B, Yershov A, Walton R, Brenner M. Chest. 2006; 130:863–868. [PubMed: 16963687]

26. Karamzadeh AM, Jackson R, Guo S, Ridgway JM, Wong HS, Ahuja GS, Chao MC, Liaw LH, Chen Z, Wong BJ. Archives of otolaryngology--head & neck surgery. 2005; 131:499–504. [PubMed: 15967882]

27. Kaiser ML, Rubinstein M, Vokes DE, Ridgway JM, Guo S, Gu M, Crumley RL, Armstrong WB, Chen Z, Wong BJ. Clinical otolaryngology : official journal of ENT-UK ; official journal of Netherlands Society for Oto-Rhino-Laryngology & Cervico-Facial Surgery. 2009; 34:460–466.

28. Roh JL, Lee YW, Park HT. The Annals of otology, rhinology, and laryngology. 2006; 115:611–616.

29. Chafin JB, Sandulache VC, Dunklebarger JL, Otteson TD, Hoffmann PJ, Hebda PA, Dohar JE. Archives of otolaryngology--head & neck surgery. 2007; 133:358–364. [PubMed: 17438250]

30. Hanauer AD, Fraga JC, Sousa JK, Sanches PR, Duarte ME, Ulbrich-Kulczynski J, Filho OH, Saueressig MG. Pediatric surgery international. 2007; 23:1227–1231. [PubMed: 17899131]

31. Richter GT, Mehta D, Albert D, Elluru RG. Archives of otolaryngology--head & neck surgery. 2009; 135:45–52. [PubMed: 19153307]

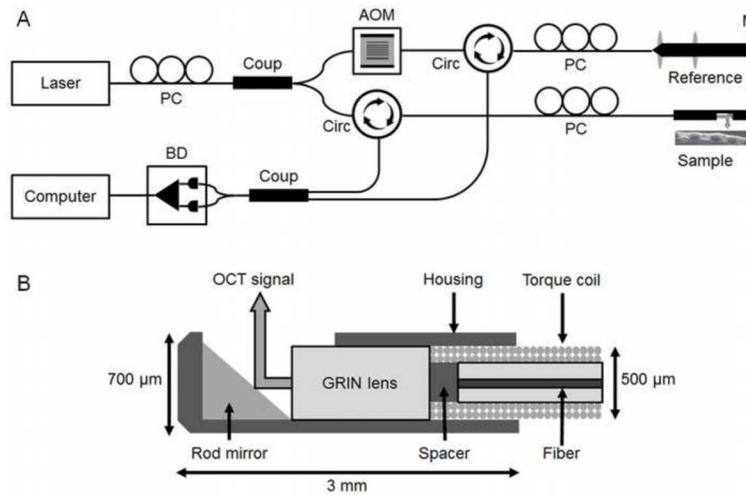32. Kelly NA, Murphy M, Giles S, Russell JD. The Laryngoscope. 2012; 122:2574–2581. [PubMed: 22961393]

Figure 1.
Schematic of long-range swept source FD-OCT system (A) and cross-section of the distal cap of the 0.7 mm outer diameter optical probe (B). PC = polarization controller, BD = balance detector, Coup = coupler, AOM = acousto-optic modulator, Circ = circulator, M = mirror, GRIN = gradient refractive index.
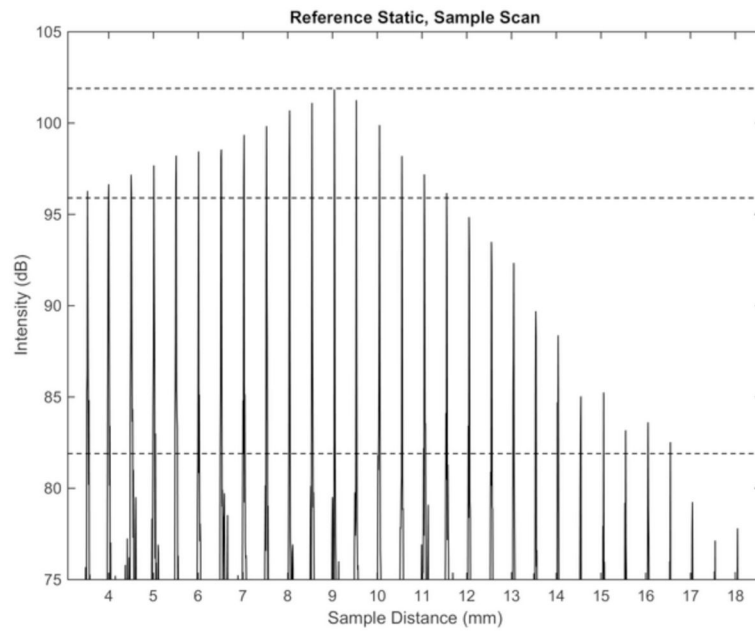
Figure 2.
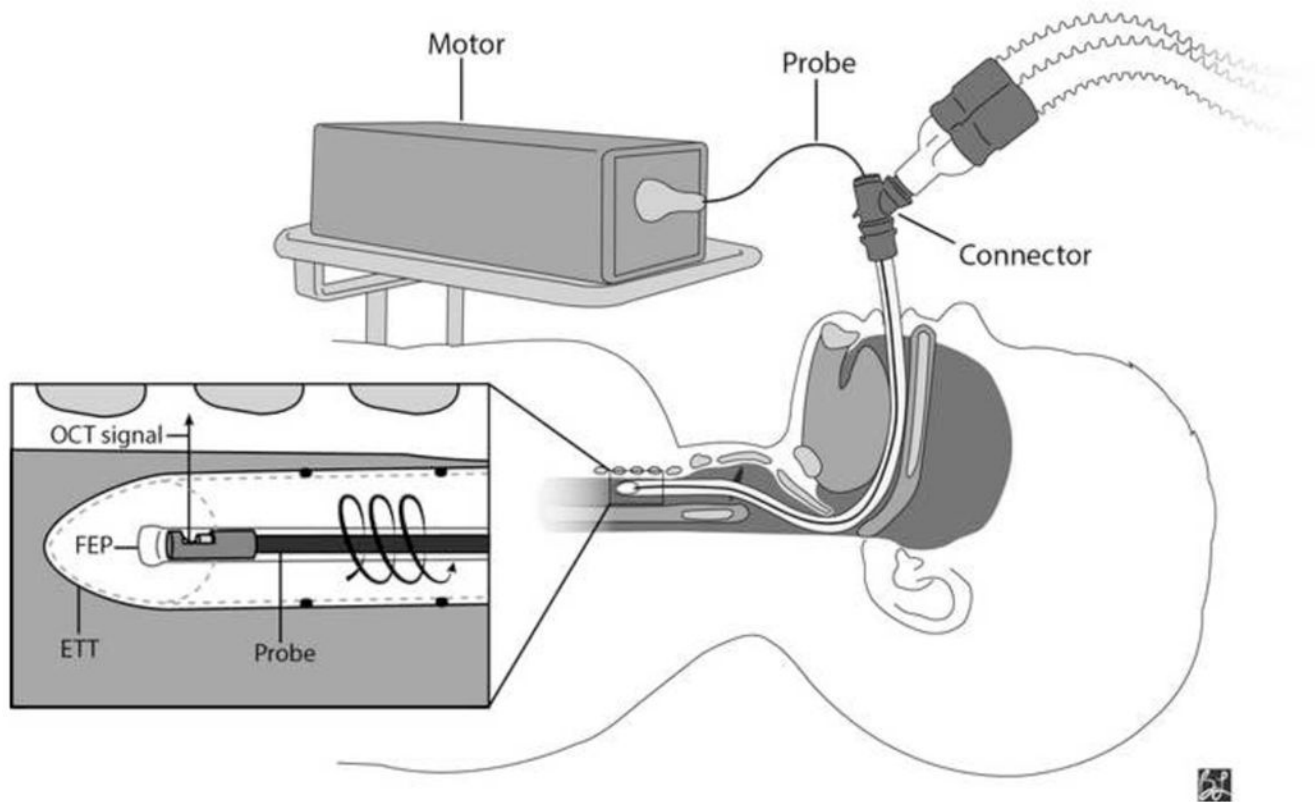Sensitivity decay of combined FD-OCT system and optical probe (9 mm focal length).

Figure 3.
Intraoperative FD-OCT of the pediatric airway. A 0.7 mm OD OCT probe (75–80 cm length) is connected to a combined rotational motor and dual-motor stage for linear pullback. The probe, housed in a transparent fluorinated ethylenepropylene (FEP) sheath, is inserted through a Y-connector and advanced inside the endotracheal tube. The combined motors simultaneously rotate and retract the probe through the upper airway as OCT signal is reflected at 90° into the tissue. ETT = endotracheal tube.
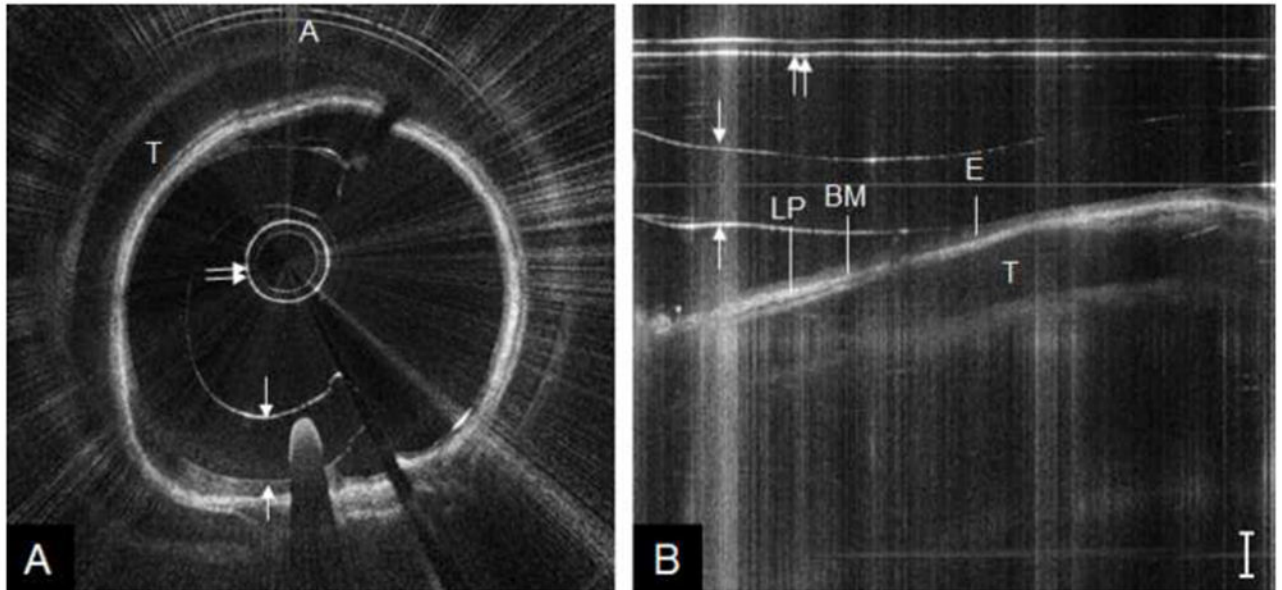
Figure 4.
OCT image of pediatric trachea, represented in polar coordinates (A) and cropped segment of Cartesian coordinates (B). A = anterior, T = tracheal cartilage, E = epithelium, BM = basement membrane, LP = lamina propria; double arrow = probe sheath, single arrows = endotracheal tube inner/outer wall. Bar = 500 μm.
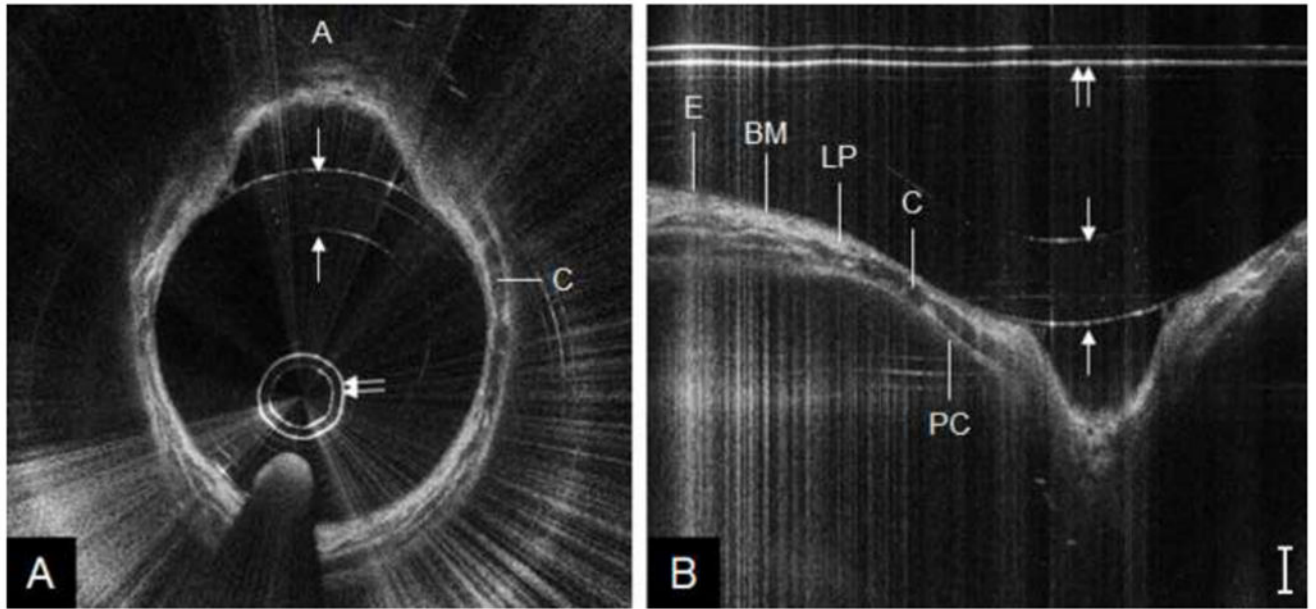
Figure 5.
OCT image of pediatric subglottis, represented in polar coordinates (A) and cropped
segment of Cartesian coordinates (B). A = anterior, C = cricoid cartilage, E = epithelium,
BM = basement membrane, LP = lamina propria, PC = perichondrium; double arrow =
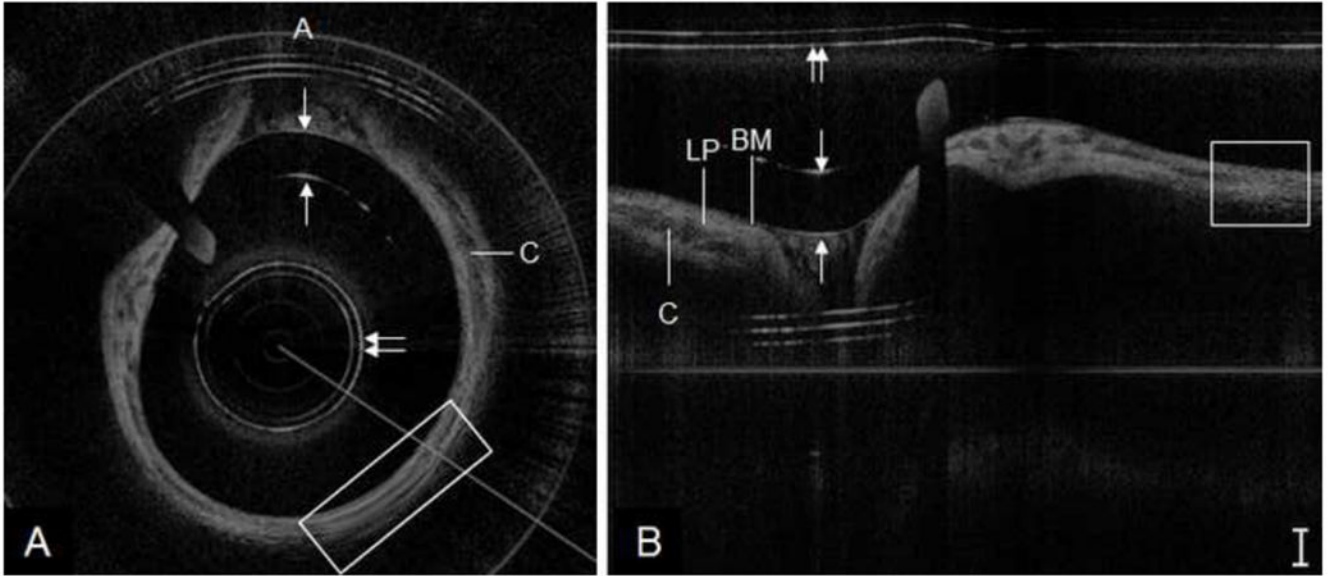probe sheath, single arrows = endotracheal tube inner/outer wall. Bar = 500 μm.

Figure 6.
OCT image of pediatric subglottis, represented in polar coordinates (A) and cropped segment of Cartesian coordinates (B). A = anterior, C = cricoid cartilage, BM = basement membrane, LP = lamina propria; box = segment of stretched data (probe rotational hysteresis), double arrow = sheath, single arrows = endotracheal tube inner/outer wall. Bar = 500 μm.
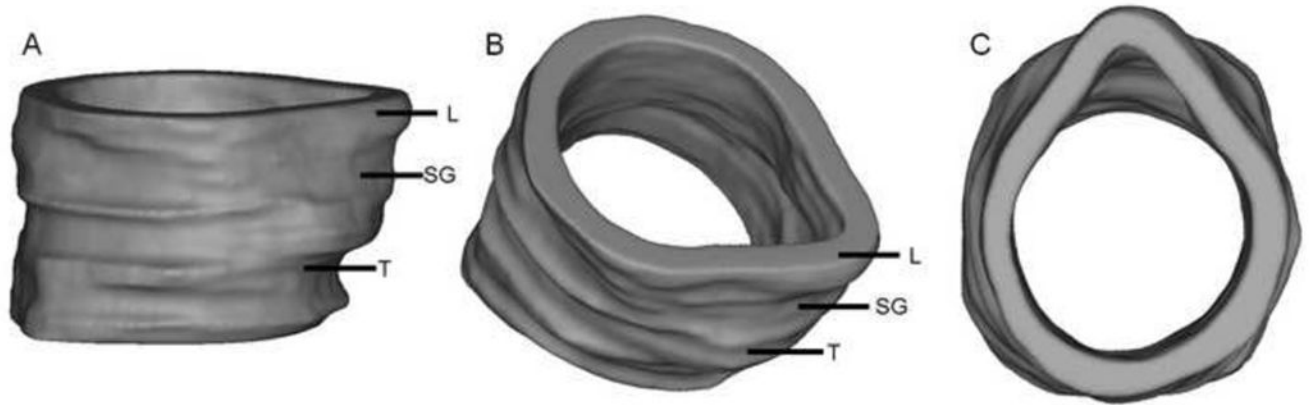
Figure 7.
3D model of pediatric lower airway created in Mimics software platform, shown in sagittal (A), oblique (B) and superior (C) orientations. L = larynx, SG = subglottis, T = trachea.
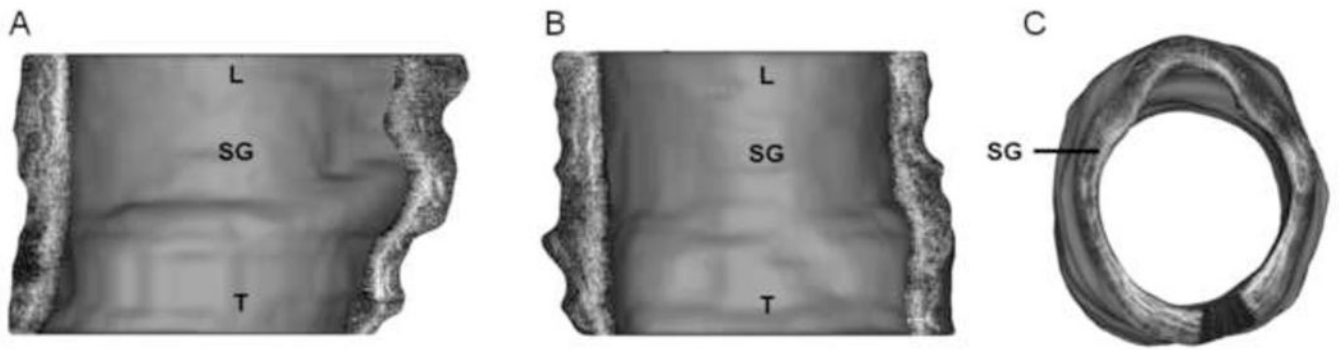
Figure 8.
Cross-sectional views of 3D model of pediatric airway, shown in sagittal (A), coronal (B) and axial (C) orientations. L = larynx, SG = subglottis, T = trachea.